Data Science Faculty Publications

School of Data Science

2024

Predicting Radiation-Induced Immune Suppression in Lung Cancer Patients Treated With Stereotactic Body Radiation Therapy

Jonathan Colen
Old Dominion University, jcolen@odu.edu

Cam Nguyen
University of Virginia

Seth W. Liyanage
Stanford University

Eric Aliotta
University of Virginia

Joe Chen
University of Virginia

Original Publication Citation

Authors

Jonathan Colen, Cam Nguyen, Seth W. Liyanage, Eric Aliotta, Joe Chen, Clayton Alonso, Kara Romano, Sean Peach, Timothy Showalter, Paul Read, James Larner, and Krishni Wijesooriya

MEDICAL PHYSICS

Predicting radiation-induced immune suppression in lung cancer patients treated with stereotactic body radiation therapy

Jonathan Colen[1,2,3] | Cam Nguyen[1] | Seth W. Liyanage[4] | Eric Aliotta[5] | Joe Chen[5] | Clayton Alonso[5] | Kara Romano[5] | Sean Peach[5] | Timothy Showalter[5] | Paul Read[5] | James Larner[5] | Krishni Wijesooriya[1,5]

[1]University of Virginia, Department of Physics, Charlottesville, Virginia, USA

[2]Old Dominion University, Joint Institute on Advanced Computing for Environmental Studies, Norfolk, Virginia, USA

[3]Hampton Roads Biomedical Research Consortium, Portsmouth, Virginia, USA

[4]Stanford University, Department of Mechanical Engineering, Stanford, California, USA

[5]University of Virginia, Department of Radiation Oncology, Charlottesville, Virginia, USA

Correspondence
Krishni Wijesooriya, Department of Radiation Oncology, University of Virginia, Charlottesville, Virginia, USA.
Email: kw5wx@virginia.edu

Funding information
National Institutes of Health, Grant/Award Number: R01CA234281; UVA Physical Sciences-Oncology Network; UVA Cancer Center

Abstract

Background: Stereotactic body radiation therapy (SBRT) is known to modulate the immune system and contribute to the generation of anti-tumor T cells and stimulate T cell infiltration into tumors. Radiation-induced immune suppression (RIIS) is a side effect of radiation therapy that can decrease immunological function by killing naive T cells as well as SBRT-induced newly created effector T cells, suppressing the immune response to tumors and increasing susceptibility to infections.

Purpose: RIIS varies substantially among patients and it is currently unclear what drives this variability. Models that can accurately predict RIIS in near real time based on treatment plan characteristics would allow treatment planners to maintain current protocol specific dosimetric criteria while minimizing immune suppression. In this paper, we present an algorithm to predict RIIS based on a model of circulating blood using early stage lung cancer patients treated with SBRT.

Methods: This Python-based algorithm uses DICOM data for radiation therapy treatment plans, dose maps, patient CT data sets, and organ delineations to stochastically simulate blood flow and predict the doses absorbed by circulating lymphocytes. These absorbed doses are used to predict the fraction of lymphocytes killed by a given treatment plan. Finally, the time dependence of absolute lymphocyte count (ALC) following SBRT is modeled using longitudinal blood data up to a year after treatment. This model was developed and evaluated on a cohort of 64 patients with 10-fold cross validation.

Results: Our algorithm predicted post-treatment ALC with an average error of $0.24 \pm 0.21 \times 10^{9}$ cells/L with 89% of the patients having a prediction error below 0.5×10^{9} cells/L. The accuracy was consistent across a wide range of clinical and treatment variables. Our model is able to predict post-treatment ALC < 0.8 (grade 2 lymphopenia), with a sensitivity of 81% and a specificity of 98%. This model has a ~38-s end-to-end prediction time of post treatment ALC.

Jonathan Colen and Cam Nguyen contributed equally.

Conclusion: Our model performed well in predicting RIIS in patients treated using lung SBRT. With near-real time model prediction time, it has the capability to be interfaced with treatment planning systems to prospectively reduce immune cell toxicity while maintaining national SBRT conformity and plan quality criteria.

1 | INTRODUCTION

Stereotactic body radiation therapy (SBRT) is an effective treatment for non-small cell lung cancer (NSCLC) that can achieve local control in more than 90% of cases.[1] Beyond its primary mechanism for tumor control, SBRT has also been shown to modulate the immune system in ways which can improve outcomes.[2,3] SBRT promotes generation of anti-tumor T-cells which may target distant metastases or residual disease not removed by the primary treatment.[4] It can also stimulate tumor-infiltrating lymphocytes (TILs), leading to a mechanism known as "soft kill," which has been shown to lead to more favorable outcomes.[5–8] However, long-term outcomes for patients treated with SBRT remain poor, with 5-year survival rates of only 42% often driven by distant failures.[9]

In addition to medical comorbidities, one potentially modifiable driver of poor long-term outcomes is radiation-induced immunosuppression (RIIS).[10,11] RIIS stems from toxicity to highly radiosensitive lymphocytes[12–15] and in severe cases can result in treatment-related lymphopenia (TRL), which has been associated with poor outcomes in numerous treatment sites.[16–19] Reducing immune suppression is a promising avenue for improving patient outcomes following SBRT, especially with the increasing concurrent use of immunotherapy and radiation for cancer patients.[20] Radiation treatments that reduce RIIS may allow more patients to be eligible for immunotherapy and may lead to improved survival following immunotherapy due to creating an immune hot environment.[21] Furthermore, since the radiation induced immune suppression is a time-dependent function, understanding the time-dependent nature of RIIS may also improve outcomes by enabling optimal timing of immunotherapy administration for maximal tumor control.[22] Specific treatment plan characteristics have been linked to immunosuppression following RT for NSCLC. In advanced stage lung cancer, PTV volume, Lung V5-V10,[10] mean thymus dose, and mean thoracic duct dose,[23] V20 of thoracic spine, lung, and heart,[24] blood rich and immune rich organs[25] have been linked to RIIS, while in early stage lung cancer thoracic spine V3,[26] heart and lung dose volumes,[27] and Heart+GV (integral dose, V5, V10, V15, V30), Thoracic spine (V1, V2, V5), lymph node stations (integral dose, V5, V10, V15) and rest of the body, external-PTV (integral dose, V1, V2, V5, V10, V15)) linked with near term RIIS, and acute long-term RIIS has been correlated with only Heart+GV (V15, V20, V40).[28] However, given the large heterogeneity in these threshold values, baseline immune status, tumor volumes, stage of the cancer and radiation treatment plans among patients, as well as the relative motion of the immune cells in the body with respect to the treatment beams, a patient-specific approach is needed.

It is well established that the irradiation of circulating blood significantly reduces absolute lymphocyte counts (ALCs).[29,30] Even a highly focused RT treatment such as SBRT can deliver a low but potentially toxic dose (> 0.5 Gy)[31] to circulating lymphocytes (CLs). Conventional RT planning and analysis tools, which aim to minimize the dose delivered to critical organs, are not equipped to reduce doses to a patient's blood pool. While these critical organs have well-defined contours and remain stationary during treatment, the blood pool is distributed throughout the body and circulates continuously. Individual blood cells can flow in and out of the irradiated field over the course of a treatment. To evaluate the dose delivered to CL for a given RT plan and estimate ALC, the dynamics of blood flow as well as time-dependent dose delivery must be considered in the planning process.

To overcome this limitation, several blood circulation modeling approaches have been proposed and implemented in the brain,[32,33] abdomen,[34] liver,[35,36] esophagus,[37] and multiorgan systems.[38–41] In the case of lung cancer, many predictive models use static organ doses as surrogates for circulating immune cells, in order to predict overall survival in the case of standard fractionation. For example, effective dose to immune cells (EDIC)[42,43] is a function of the number of RT fractions, the integral dose to the entire body, and the mean dose delivered to the lung and heart. Subsequent improvements to EDIC accounted for the mean dose to the thymus and thoracic duct[23] to calculate the change in ALC (DALC) after radiation therapy. Other approaches have used cardiopulmonary organ dose volumes to predict overall survival[44] or used gross tumor volumes, chemotherapy status, and BID treatment status[10] to predict the nadir point of post-treatment ALC.

These models offer promising insights into how RIIS affects overall survival, as well as its correlation with different treatment modalities and organs. However, they have some limitations that limit their use as a patient-specific model for predicting immune levels following

lung SBRT. In this case, dose fractionations are 3–5 days and patients' immune levels vary rapidly after treatment, unlike standard fractionations where immune suppression is smoothly varying over time. Accurate predictions of time-dependent immune levels will help improve survival outcomes. For example, they may be valuable in deciding the optimum time window for administering immunotherapy. Additionally, a model that accounts for blood flow with organ-specific blood flow velocities in the thorax, as well as time-dependent lymphocyte replenishment, will be of great value due to its accuracy and flexibility in handling other individual organs.

The purpose of this work was to develop a model that predicts long-term acute RIIS for lung SBRT by estimating the dose delivered to circulating blood lymphocytes. The algorithm models dose within all organs in the thorax surrounding the treatment area up to a threshold of 40 cGy per fraction (It has been reported that 50 cGy is a threshold for lymphocyte kill[32]) and accounts for patient-specific anatomy, treatment plan, and baseline immune status to predict time-dependent post-treatment ALC. We aimed to develop this model to interface with treatment planning systems (based on DICOM format) and generate fast predictions to augment decision making during treatment planning.

2 | METHODS

2.1 | Dynamic delivery simulation

This model included three key components—(i) a simulation of dynamic dose delivery to blood flowing through key organs with random mixing of blood outside the radiation dose area, (ii) a dose-dependent cell kill model, and (iii) a time-dependent lymphocyte death and regeneration model. Blood flow dynamics were modeled using a Monte-Carlo style simulation in which local flow velocities were determined using published organ-specific cardiac outputs[45,46] and organs' cross-sectional areas in patient-specific CT images. The dynamic dose delivery model extracted RT treatment plans, CT planning image sets, dynamic dose distributions, and contoured organ structure sets from DICOM format files in order to determine time-dependent radiation doses for each voxel of each organ of interest. The simulation modeled a pool of CLs, which flowed through each organ and accumulated a distribution of radiation doses. This accumulation was a function of each lymphocytes position in space, dictated by the blood-flow model, and the time-dependent radiation dose from the treatment plan. This was used to determine initial cell kill via a dose-dependent model following published data.[47] Finally, time-dependent lymphocyte regeneration and death was determined using a model fit to patient measurement data, as described

below. Each component of the model is described in detail in the following sections.

2.2 | Blood flow simulation

The pool of CL was simulated using a total blood volume of 5 L, which moves through the patient's body assuming a heart-to-heart circulation time (H2H) of 60 s. This is defined as the time it takes for blood to cycle from the left ventricle, throughout the body (the systemic circulation), then back to the right atrium and right ventricle of the heart, then to the lungs to exchange oxygen and carbon dioxide (the pulmonary circulation), and finally return to the left atrium of the heart. The simulation computes the blood flow through each organ separately, to account for differences in organ size and the rate of blood flow through each organ. For each organ, the blood flow velocity is determined by the Equation 1:

$$v = \frac{5000\,(cm^3) \times CO}{H2H\,(s) \times \left[BVD \times A_{CS}\,(cm^2)\right]}\,(cm/s) \quad (1)$$

Here, CO is the cardiac output percentage, which describes the fraction of total cardiac output flowing to an organ. BVD is the blood volume density, or the volume percentage of an organ that is filled with blood. A_{cs} is the average axial cross-sectional area of the organ, and the product ($BVD \times A_{cs}$) is the amount of blood that is contained in that axial slice of that organ. By using an approach based on the cross-sectional area of each organ, we were able to model blood flow through complex organ shapes that would be accurate on average over the course of a full treatment.

Using this approach, we simulated the following regions: individual great vessels (aorta, vena cava, pulmonary artery), lungs, heart, liver, spleen, and stomach in the case of tumors in the lower thorax. We also modeled flow through "other organs" (a cartoon depiction of the thorax is shown in Figure 1 top left) by subtracting the above regions from the total external contour. Given a set of voxels S inside the patient, and a set O of organs already contoured, the "other organs" were given by $S_{other} = S - \cup_{i \in O} S_i$. For each organ, A_{cs} was computed using the patient's CT images, while CO was obtained from published results.[45,46] The cardiac output for "other organs" was given by $CO_{other} = 1 - \sum_{i \in O} CO_i$. For great vessels, lungs, and the heart, we used $CO = 100\%$, as all blood passes through them with each circulation. This resulted in great vessel average blood velocities of ~8.7 cm/s for aorta, ~13.4 cm/s for vena cava, and 7.3 cm/s for pulmonary artery, which are close to published values.[48,49]

The radiation dose delivery to the CL pool was simulated over time by dividing the total dose from each
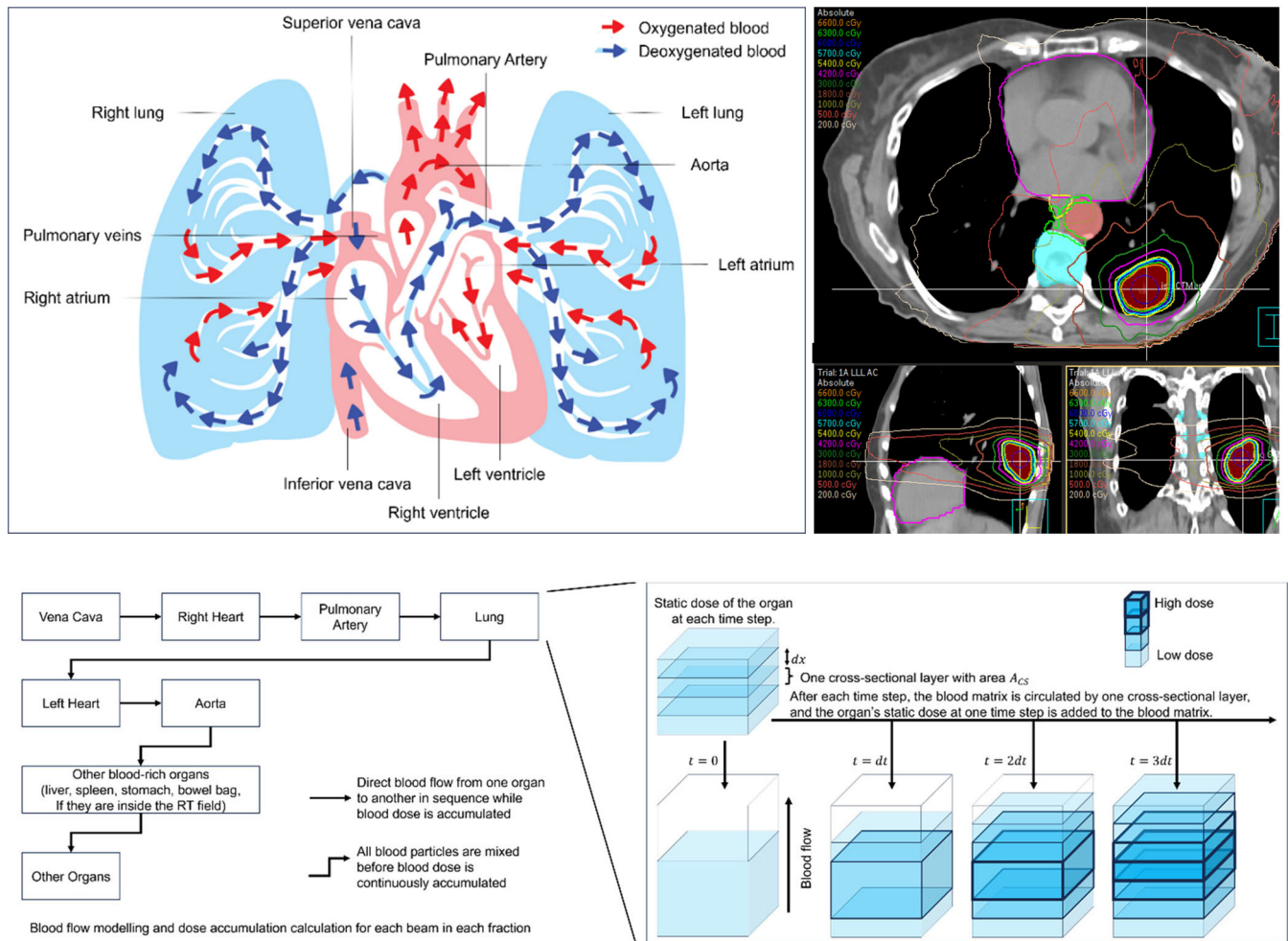
FIGURE 1 Top (Left) Blood flow in the thorax and through the blood rich organs (heart and great vessels) and the transfer between the heart and the lungs that is used in the model. Top (Right) An actual lung SBRT patient simulated with all organs to show the inclusion of all organs in the thorax. Bottom shows a flow chart showing the workings of the predictive algorithm in increments of space (dx), and increments of time (dt). The right-hand bottom shows the blood flow through an organ at different time steps, with the irradiated blood at the previous time step has been moved up.

treatment beam into fractions and subsequently into discrete time-steps. This time interval, dt, was organ dependent and defined by the time required for a circulating cell to traverse an image voxel:

$$dt = \frac{dx}{v} \quad (2)$$

Here, dx is the voxel length of 2.5 mm and v is the organ-specific blood velocity defined above. The dose from each beam was then divided into $N_{seg} = T/dt$ segments where T is the time required to deliver the entire beam. Each beam segment was further divided into doses delivered to the individual organs listed above. This was done by applying logical masks from the contoured structure sets and enabled the dose to be applied to each structure while avoiding leakage into other organs. For a given organ O, the dose delivered in one beam segment can be computed using the dose

D of a single beam for a single treatment fraction and the organ's spatial mask $mask_O$.

$$D_O = \frac{D[mask_O]}{N_{seg}} \quad (3)$$

The total blood volume was modeled by a blood matrix of size $N \times 1$, where $N = \frac{5000 cm^3}{0.25 \times 0.25 \times 0.25\ cm^3} = 320\,000$ blood particles and $0.25 \times 0.25 \times 0.25 cm^3$ is the volume of each dose voxel from the treatment planning system dose map. For each organ, the contoured logical mask was applied to the blood matrix to ensure that dose was only applies to the section of blood "inside" the organ at a given time. Every dt seconds, the dose for a given beam segment and organ was applied and the blood matrix was circulated by one organ cross-sectional layer in the superior-inferior direction. During the time required to deliver the entire beam, the blood matrix entries, and the

CL they represent, accumulate radiation dose as they move through each organ. We repeated this process for each organ listed above, including the "other organs," for each beam and each treatment fraction in the patient's plan. Between each beam and treatment fraction, the blood matrix was shuffled to simulate the mixing of blood throughout the body. The result was a blood matrix whose entries captured the dose accumulated by CL in the patient's blood pool over the course of a radiation therapy treatment. Figure 1 (bottom) represents the model structure schema and blood matrix dose accumulation due to blood flow through the radiation beam in space and time.

2.3 | Lymphocyte toxicity $K(t)$ simulation

To translate accumulated dose into cell death fractions, we used a kill function $K(D_i)$, where D_i is an entry of the blood matrix representing the dose accumulated by an individual CL after a radiation treatment is administered. We used a linear-quadratic (LQ) model[50] for lymphocyte kill:

$$K(D_i) = 1 - e^{-\left(\alpha D_i + \beta D_i^2\right)} \quad (4)$$

Because in vivo lymphocyte radiotoxicity data is not readily available, the parameters α, β were fit to published in-vitro survival curves from Nakamura et al.[47] ($\alpha = 0.255, \beta = 0.147$). This model predicts 15% kill for a dose of 0.5 Gy, 33% kill for a dose of 1 Gy, 67% kill for a dose of 2 Gy, and 88% kill for a dose of 3 Gy. Cumulative dose to CLs has a wide range from 0 to D_{max}, and the total lymphocyte kill is

$$K_0 = \sum_{D_i=0}^{Dmax} N_i \left(1 - e^{-\left(\alpha D_i + \beta D_i^2\right)}\right)$$

$$= N_0 - \sum_{D_i=0}^{Dmax} N_i e^{-\left(\alpha D_i + \beta D_i^2\right)} \quad (5)$$

Here N_i are the number of cells receiving dose D_i, and $N_0 = \sum_{D_i=0}^{D_{max}} N_i$ is the pre-treatment ALC value.

2.4 | Modeling time-dependent ALC

Figure 2 shows the functional form used to predict ALC over time following treatment. The patient's lymphocyte count as a function of time is given by Equation 6 where $K(t)$ is a time-dependent function for lymphocyte toxicity, and $R(t)$ is a time-dependent function for lymphocyte regeneration.
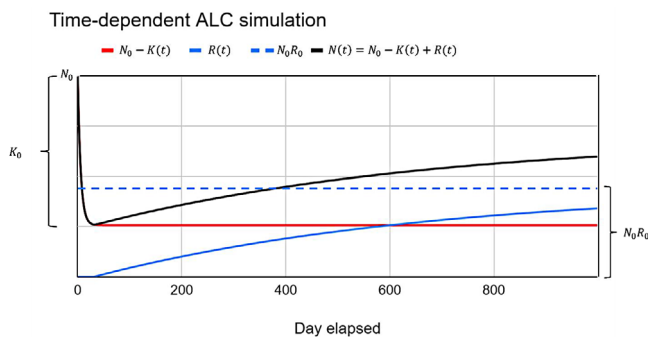

FIGURE 2 The time-dependent form of cell kill term $K(t)$, recovery term $R(t)$, and final prediction $N(t)$.

$$N(t) = N_o - K(t) + R(t) \quad (6)$$

$$K(t) = K_0 \times \left(1 - e^{-at}\right) \quad (7)$$

$$R(t) = N_0 \times R_0 \times \left(1 - e^{-b(t-30)}\right) \; if \, t \geq 30$$
$$and \; R(t) = 0 \; if \, t < 30, \quad (8)$$

Cumulative ALC data from patient blood draws was used empirically to model the time-dependent lymphocyte function. It exhibits an exponential decay up to a time of 30 days where we observe a nadir point, and a gradual replenishment afterwards following lung SBRT.[51] Swanson et al. also found a nadir point in absolute lymphocyte reduction around four week time point for different types of cancers treated with standard fractionation RT.[52] We modeled the measured time dependence of lymphocyte kill and recovery using two exponential functions: (i) a time-dependent kill function with Equation 7, where a is an unknown decay constant and t is the number of days elapsed since radiotherapy treatment initiation; and (ii) a time-dependent replenishment rate $R(t)$, which represents the release of new lymphocytes into the bloodstream from primary and secondary lymphoid organs over time, as well as the proliferation of new cells which depends on the pre-treatment immune status of a given patient. We assume replenishment occurs following the nadir at 30 days, and model it empirically using Equation 8. Here, R_0, b are parameters to be estimated empirically from available longitudinal blood draw data.

Model parameters a, b, and R_0 were optimized to minimize the χ^2 difference between simulated lymphocyte survival fractions and measured blood-draw data across our patient cohort using a 10-fold cross-validation process. The cohort was segmented into ten distinct groups, and ten models were fit using 90% of the patients to optimize and evaluated using the remaining 10%. This process allowed us to evaluate model

performance on all available data while avoiding overlap between training and test sets. When comparing post-treatment ALC between the output of our model and measurement, we projected the regeneration from the nadir point to the measured ALC date for each patient.

2.5 | Patient cohort

Patients who underwent SBRT for NSCLC were included in this institutional review board approved retrospective analysis. Imaging volumes and SBRT treatment plans collected for 64 patients in total were used to optimize and validate the model. Table 1 describes the characteristics of measurement data (patient, dosimetric, and ALC) used for this study, with the blood-rich organ (heart + great vessels) dose levels that has shown to significantly correlate with post SBRT ALC loss. All plans were optimized to meet the dosimetric criteria defined in the radiation therapy oncology group (RTOG) 0915 (for peripheral tumors, 59.4% of patients)[53] or 0813 (for centrally located tumors, 40.6% of cases)[54] protocols. All plans were designed for delivery on a Varian linear accelerator using either a step-and-shoot intensity-modulated radiation therapy (IMRT) (67.2% of plans), a volumetric-modulated arc therapy (VMAT) delivery (29.7% of plans), or a three-dimensional conventional radiation therapy (3D-CRT) delivery (3.1% of plans).

2.6 | Organ-at-risk contouring

The following organs-at-risk (OAR) were manually contoured by a set of trained physicians following the RTOG atlas for organs at risk in thoracic radiation therapy, encompassing a region of interest up to a very low threshold dose of 40 cGy per fraction): lungs, great vessels (aorta, vena cava, pulmonary vessels), heart, liver, spleen, and stomach (only for lower thorax tumors). All remaining tissue in the body was combined to a region denoted "Other Organs." Example masks showing this discretization are shown in Figure 1 top right.

2.7 | Lymphocyte measurements

ALC measurements were recorded pre-treatment and at multiple post-treatment time points. Post-treatment lymphocyte count drops were determined by computing the difference between the first post-treatment ALC and the pre-treatment baseline ALC. Having post-treatment blood data at different time points helps define the time dependence of the predictive model.

2.8 | Model accuracy

Model accuracy was assessed by comparing predicted post-treatment ALC with those measured in the post-treatment blood draws. Accuracy was assessed for each patient in the test sets created during the survival function cross-validation process. Differences in prediction accuracy in the presence of specific plan characteristics (tumor location, tumor volume, radiation delivery method, and treatment time) were evaluated to identify systematic errors.

The model was also assessed in terms of its rate of immune suppression prediction accuracy using the cumulative distribution function (CDF). CDF is defined by the probability that the prediction accuracy will have a value less than or equal to a given difference of measurement to prediction.

2.9 | Dose-level contributions to lymphocyte kill

To identify the dosimetric drivers of lymphocyte toxicity, we compared contributions to cell kill from different blood dose levels. This is important to assess whether RIIS is driven primarily by focused high-dose regions or distributed low doses. The kill contribution $C(D)$ of dose D for a given patient is given by Equation 9:

$$C\,(D) = \frac{K\,(D) \times P\,(D)}{\sum_d K\,(d)\,P\,(d)} \tag{9}$$

where $K(D)$ is the lymphocyte kill function value at dose D and $P(D)$ is the percentage of blood cells receiving dose D. D was binned with a resolution of 0.1 Gy.

2.10 | Dependence of treatment/patient characteristics on immune suppression model

To validate the model's ability to correlate the post-treatment RIIS with key patient/plan characteristics that is observed in the measurement, we evaluated the Spearman correlation functions between predicted post-treatment ALC and five variables: pre-treatment ALC, minimum distance between PTV and heart, days elapsed from treatment initiation to post-treatment ALC measurement, PTV volume, and treatment delivery time. We also evaluated correlations between patient measurements and each variable and compared them to our model predictions. To evaluate systematic differences between patient/plan characteristics, differences in cell kill contribution were

TABLE 1 Patient and dosimetric characteristics.

Characteristic		All patients ($n = 64$)
Gender	Male	28
	Female	36
Age	median (range), years	72.5 (50–92)
Race	Caucasian	53
	African American	7
	Asian	1
	Other	3
PTV volume	median (range), cc	29.34 (4.76–403.15)
RT scheme	12 Gy x 5Fx (BED[a] = 132 Gy)	32
	11 Gy x 5Fx (BED = 115.2 Gy)	1
	10 Gy x 5Fx (BED = 100 Gy)	25
	09 Gy x 5Fx (BED = 85.5 Gy)	3
	18 Gy x 3Fx (BED = 151.2 Gy)	2
	17 Gy x 3Fx (BED = 137.7 Gy)	1
RT site	Central	26
	Peripheral	38
Pre-tx ALC	median (range), 10^9 cells/L	1.68 (0.61–3.19)
Lung volume	median (range), cc	3621 (1649–6433)
Lung mean dose	median (range), Gy	4.20 (0.88–7.67)
Heart volume	median (range), cc	696 (310–1624)
Heart mean dose	median (range), Gy	1.45 (0.02–8.99)
Body volume (External)	median (range), cc	24263 (12 758–42 913)
Body mean dose	median (range), Gy	1.61 (0.77–4.24)
Heart + GV[b] mean dose	median (range), Gy	2.93 (0.15–8.94)
Heart + GV integral[c] dose	median (range), Gy.cm^3	2389 (72–10 291)
Heart + GV V5[d]	median (range), cc	154.1 (1.9–671.0)
Heart + GV V10	median (range), cc	61.3 (0.0–405.5)
Heart + GV V15	median (range), cc	19.4 (0.0–217.3)
Heart + GV V20	median (range), cc	4.1 (0.0–105.4)
External-PTV mean dose	median (range), Gy	1.53 (0.73–3.37)
External-PTV integral dose	median (range), Gy.cm^3	36978 (14234–86461)
External-PTV V1	median (range), cc	4613 (1611–10368)
External-PTV V5	median (range), cc	2035 (845–4464)
External-PTV V10	median (range), cc	1125 (253–3365)
External-PTV V15	median (range), cc	601 (109–2122)

[a]BED refers to the biologically effective dose.
[b]GV refers to the great vessels (aorta, vena cava, and pulmonary artery) combined.
[c]Integral dose refers to the volume integral of the dose deposited in the patient and is equal to the mean dose times the volume.
[d]Vx refers to the percentage of the volume that received at least x Gy radiation dose.

compared between the above five parameters as well as age of the patient, treatment modality (step-and shoot IMRT/ 3D/ arc deliveries), and tumor location (central/peripheral).

3 | RESULTS

For a typical lung SBRT plan, 320 000 blood particles were simulated and propagated through and out of the
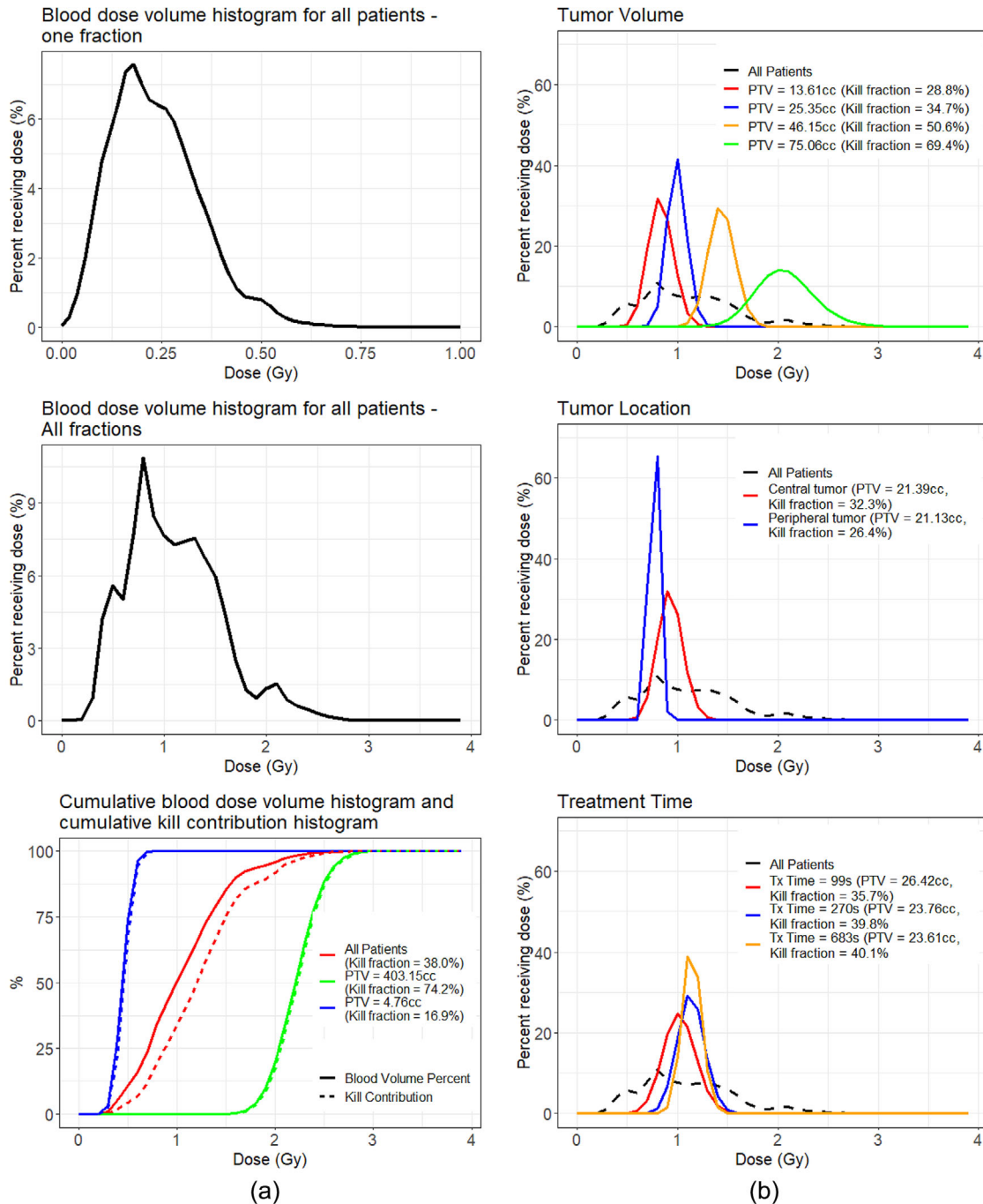
FIGURE 3 (a) Average cumulative blood dose histogram for all patients after one fraction (top, bin width = 0.02 Gy) and after all fractions (center, bin width = 0.1 Gy). Bottom: cumulative blood dose volume histograms and the corresponding cumulative cell kill contributions for two sample largest and smallest PTV volumes and for all patients. (b) Cumulative blood dose histogram for sample patients with different PTV volumes (top), different tumor locations (center) and different treatment delivery times (bottom).

dose volume. Typical times to compute post-treatment ALC were 12-field 3D plan (23 s), 11-field IMRT plan (37 s), and 2-arc VMAT plan (37 s). These short simulation times indicate that the model could interface with the treatment planning system and provide near-real time feedback to optimize plans with immune suppression considerations.

3.1 | Accumulated blood dose distribution

The model predicts a distribution of radiation doses accumulated by the patient's blood pool. Figure 3a top shows the average distribution for all patients after receiving a single treatment fraction. The mean
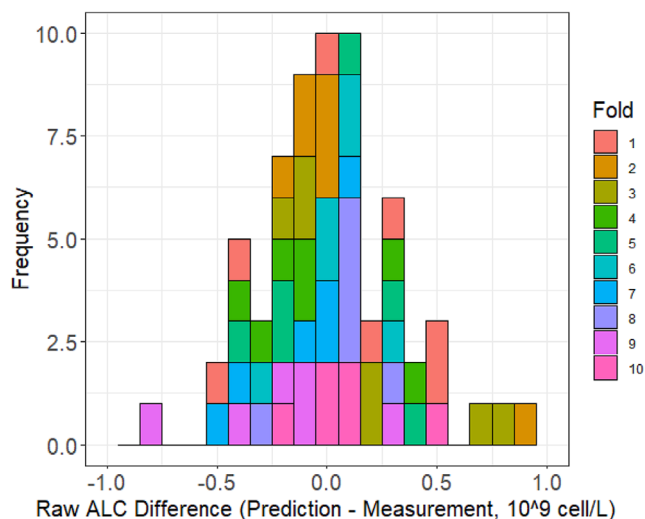
FIGURE 4 Histogram of the ALC difference (prediction—measurement) of all patients and which fold the prediction is on from the 10 folds.

accumulation is low (0.25 Gy), although it increases after all five treatment fractions have been administered (1.15 Gy, see Figure 3a middle). These plots combine the individual dose distributions for each patient in the cohort, which are narrowly distributed around different mean values.

The location and width of the blood dose distribution are determined by several factors. Patients with larger PTVs accumulate higher blood dose levels (example in Figure 3b top four PTV volumes: < 20 cc, between 20 and 40 cc, between 40 and 60 cc and > 60 cc), due to larger treatment fields, leading to larger volumes of radiation dose exposures. The location of the tumor in the lung also has an effect, with central tumors resulting in higher dose accumulation than peripheral tumors (Figure 3b middle). This occurs due to the closer proximity to great vessels and heart, which have a higher blood density than surrounding tissue in the case of central tumors. For all subgroups

of the patient cohort, the prediction fraction of blood receiving greater than 3 Gy (corresponding to the highest kill fraction reported in Nakamura et al.[47]) was negligible.

3.2 | Dose-level contributions to lymphocyte kill

The LQ model (Equation 4) converts the accumulated dose distribution into an initial lymphocyte kill fraction. Using the kill contribution metric (Equation 9), we evaluated the delivered dose regions which led to the highest lymphocyte reduction. In most cases, the highest percentage of lymphocyte toxicity for lymphocytes in the circulating blood pool came from doses around 1.5 Gy. As Figure 3a bottom shows, for all patients combined, lymphocyte toxicity was dominated by low dose levels (33.7% of toxicity came from doses <1 Gy, 75.3% of toxicity came from dose <1.5 Gy) despite the lower cell kill probabilities at these levels. Only 8.2% of the lymphocyte toxicity came from cells absorbing more than 2 Gy.

3.3 | Predicted absolute lymphocyte counts

Using our time-dependent ALC model (see Methods), we forecasted each patient's ALC at their respective post-treatment measurement days. The model was fit and tested using a ten-fold cross validation procedure. The model parameters for (a,b, and R_0) and accuracy for each iteration are given in Table 2. The histogram for the raw absolute ALC difference (prediction—measurement) is shown in Figure 4, with the color indicating which fold one particular ALC difference was on.

Figure 5 compares post-treatment ALC model predictions to patient measurements. The left panel plots

TABLE 2 Results of optimized parameters and prediction accuracy for the training and testing set for each of the 10 folds.

Fold	N train	N test	a (day^{-1})	R_0	b (day^{-1})	ALC Difference between prediction and measurement (10^9 cell/L)			
						Mean—training	SD—training	Mean—testing	SD—testing
1	57	7	0.5261	0.7020	0.0009	0.21	0.15	0.35	0.15
2	57	7	0.5261	0.7020	0.0009	0.23	0.31	0.20	0.31
3	57	7	0.5261	0.7022	0.0014	0.22	0.27	0.33	0.27
4	57	7	0.5261	0.7020	0.0009	0.22	0.12	0.26	0.12
5	58	6	0.5276	0.7295	0.0009	0.23	0.10	0.26	0.10
6	58	6	0.5263	0.8009	0.0012	0.24	0.10	0.14	0.10
7	58	6	0.5261	0.7049	0.0008	0.23	0.19	0.19	0.19
8	58	6	0.5262	0.7054	0.0009	0.23	0.09	0.18	0.09
9	58	6	2.9997	0.8040	0.0007	0.22	0.24	0.30	0.24
10	58	6	0.5261	0.7020	0.0014	0.24	0.17	0.18	0.17
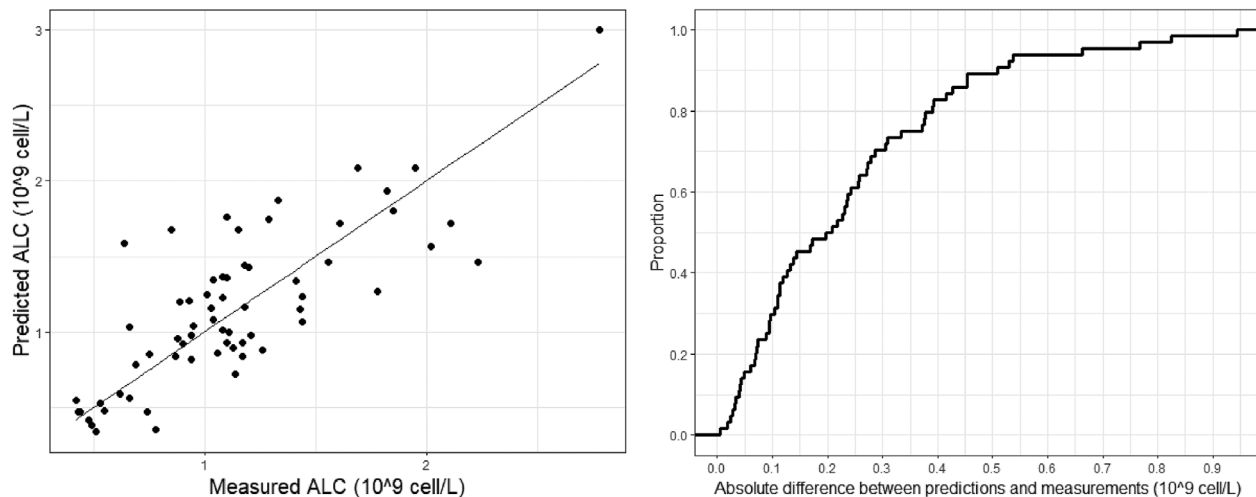
FIGURE 5 Left: Predicted post-treatment ALC count as a function of measured ALC count. Right: Cumulative distribution function (CDF) showing the proportion of patients with a given prediction accuracy.

the predicted post-treatment ALC against the measured ALC count. The right panel shows the CDF (CDF of patient predictions achieving a given accuracy. Predictions differed from measured values by an average (SD): 0.24 (0.21) $\times 10^9$ cell/L (or 13.7% (10.3%) compared to pre-treatment ALC). Eighty-nine percent of the patients have a difference between prediction and measurement smaller than 0.5×10^9 cells/L. The measured pre-treatment ALC values have a mean (range) of 1.68 (0.61–3.19). Our model's mean error rate is lower than half of the lowest ALC value, indicating it has sufficient sensitivity to detect whether a patient is expected to develop treatment-related Grade 3 lymphopenia (post-treatment ALC < 0.5 lymphopenia per NCI guidelines). Our model is able to predict post-treatment ALC < 0.8 (grade 2 lymphopenia), with a sensitivity of 81%; and a specificity of 98% (Due to the low statistic, we decided to test G2 lymphopenia as opposed to G3 lymphopenia). The mean (STD) for the difference between prediction and measurement over the 10 folds for different sub-groups (pre-treatment ALC, age, treatment modality, post-treatment blood draw time point, tumor location, treatment delivery time, and tumor volume) are shown in Table 3.

3.4 | Prediction accuracy dependence on patient and delivery characteristics

Different key treatment plan/patient characteristics can affect RIIS differently. To validate the model further, we next evaluated whether the model predictions recreate observed relationships between plan characteristics and RIIS. Figure 6 shows post-treatment ALC as a function of five variables. The left column shows the post-treatment ALC as a function of the plan charac-

teristics for both measurement and simulation and the right column plots the model accuracy (absolute difference between prediction and measurement). Variables shown are (A) pre-treatment ALC, (B) minimum distance between PTV and heart, (C) days elapsed from treatment initiation to post-treatment ALC measurement, (D) PTV volume, and (E) treatment delivery time. We did not observe a trend between any of these plan characteristics and predictive accuracy. Some notable observations from these comparisons were:
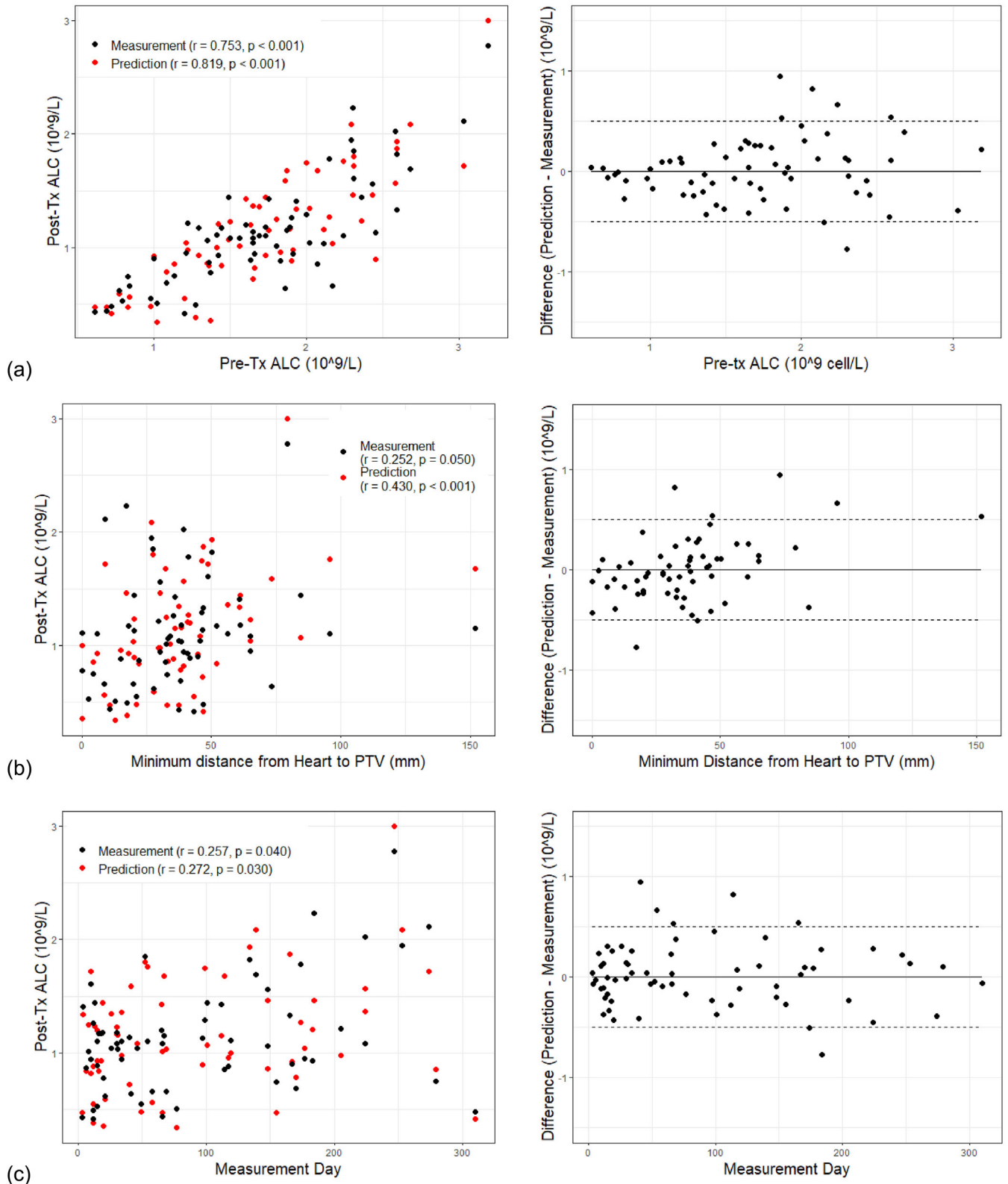
3.4.1 | Pre-treatment ALC

As the pre-treatment ALC increases, post-treatment ALC values also increase significantly for both the measurement [$r = 0.75$ ($p < 0.001$)] and the prediction [$r = 0.82$ ($p < 0.001$)].

3.4.2 | Minimum distance between PTV and heart

Patients whose PTV is further from the heart accumulate lower RT dose in the blood-rich organs, leading to higher post-treatment ALCs [$r = 0.25$ ($p = 0.05$)]. The model correctly predicts a positive correlation between the minimum PTV-heart distance and post-treatment ALC [$r = 0.43$ ($p < 0.001$)].

3.4.3 | Days elapsed from treatment initiation to post ALC measurement

Regeneration (Equation 7) leads to higher measured ALCs [$r = 0.26$ ($p = 0.04$)] at later measurement days.

FIGURE 6 Left-Post-treatment ALC as a function of some key plan characteristics for both measurement and simulation. The Spearman's correlation coefficient r and p-value between the measured and predicted ALC and plan characteristic); Right- model accuracy—absolute difference between prediction and measurement as a function of there variables. (a) pre-treatment ALC; (b) minimum distance between PTV and heart; (c) days elapsed from treatment initiation to post ALC measurement; (d) PTV volume; and (e) treatment delivery time.
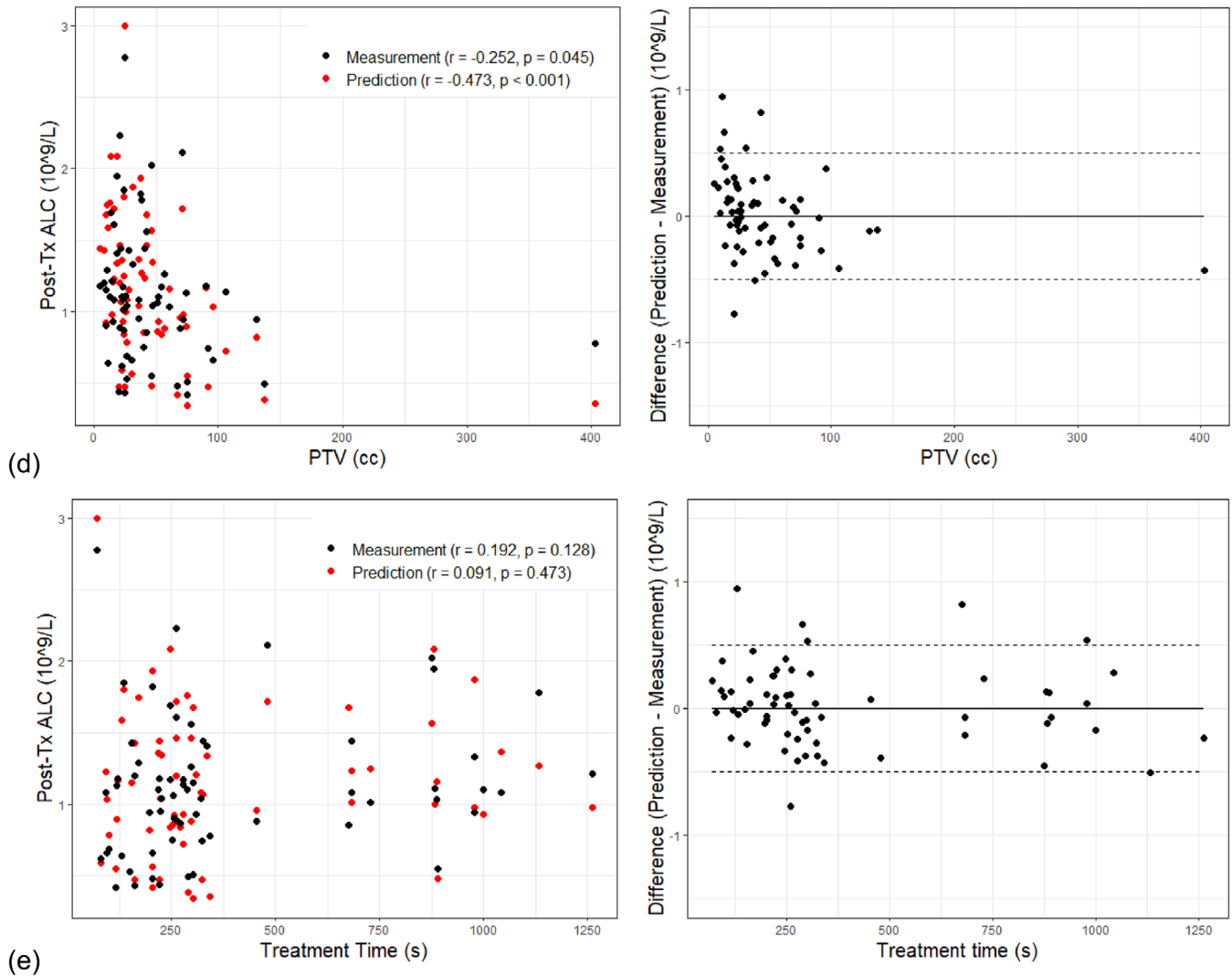
(d)

(e)

FIGURE 6 Continued

The model predictions capture this positive correlation [$r = 0.27$ ($p = 0.03$)].

3.4.4 | PTV volume

Patients with larger PTV receive larger volumes of all doses, leading to higher dose accumulation and lower post-treatment ALC [$r = -0.25$ ($p = 0.04$)]. The model predictions capture this negative correlation [$r = -0.47$ ($p < 0.001$)].

3.4.5 | Treatment delivery time

There is no observed trend with post-treatment ALC in measurement [$r = 0.19$ ($p = 0.13$)] or prediction [$r = 0.09$ ($p = 0.47$)] with treatment delivery times varying from 99 to 683 s at these low number of treatment fractions.

4 | DISCUSSION

In this work, we have presented a model which predicts radiation-induced lymphocyte reduction following lung SBRT by simulating the dose delivered to CLs in the bloodstream. This approach is patient-specific, using three-dimensional dose maps from treatment planning software, varied treatment times, and organ-specific blood flows. Our model predicts initial lymphocyte death using a linear-quadratic survival curve from literature and predicts time-dependent lymphocyte replenishment based on patients' baseline immune status. The model could accurately predict post-treatment ALC on an independent test patient dataset, with an average absolute error of $0.24 \pm 0.21 \times 10^9$ cells/L and 89% of patients having an error below 0.5×10^9 cells/L. Our model also predicts relationships between patient/treatment characteristics and measured lymphocyte depletion that are consistent with previous observations. This includes

TABLE 3 A summary of the mean (STD) for the difference between prediction and measurement over the 10 folds of the predictive model within each subset of variables.

	Absolute difference (10^9 cells/L)	Percent difference (%)	Count
Pre Tx ALC (10^9 cells/L)			
<1.0	0.08 (0.08)	9.4 (9.9)	8
1.0–1.5	0.18 (0.12)	14.1 (8.3)	16
1.5–2.0	0.24 (0.22)	14.0 (11.7)	20
≥2.0	0.35 (0.23)	15.0 (10.6)	20
Age			
<67	0.27 (0.23)	14.8 (12.0)	16
67–73	0.23 (0.14)	14.4 (8.2)	16
73–80	0.25 (0.27)	14.7 (13.4)	14
≥80	0.22 (0.18)	11.4 (7.6)	18
Modality			
3D-CRT	0.15 (0.08)	10.0 (1.7)	2
IMRT	0.26 (0.20)	14.8 (10.0)	43
Arc	0.20 (0.22)	11.7 (11.2)	19
Measurement day			
<30	0.18 (0.13)	11.7 (8.0)	19
30–180	0.26 (0.24)	14.5 (11.8)	35
≥180	0.29 (0.21)	15.0 (8.2)	10
Tumor location			
Central	0.19 (0.14)	11.9 (7.7)	26
Peripheral	0.27 (0.23)	15.0 (11.6)	38
Treatment time (s)			
<200	0.21 (0.24)	11.8 (12.1)	16
200–300	0.23 (0.20)	13.5 (8.8)	23
≥300	0.27 (0.20)	15.2 (10.5)	25
Tumor volume (cc)			
<20	0.30 (0.26)	16.3 (12.9)	15
20–40	0.21 (0.19)	11.8 (8.8)	23
40–60	0.29 (0.22)	15.3 (10.0)	11
≥60	0.20 (0.14)	12.9 (9.9)	15

Variables considered are Pre-treatment ALC count, age, treatment modality, day of post-treatment blood draw, central vs peripheral, treatment delivery time, and PTV volume size.

positive correlations between post-treatment ALC and measurement day as a result of lymphocyte replenishment following a nadir point,[26–28] and negative correlations between post-treatment ALC and target size,[35,55] as well as heart proximity to PTV.[10,24,27] A strength of this blood circulation model is that it was developed and validated using patient-specific data to predict immune suppression.

Existing modeling approaches for RIIS belong to three categories: dose volume-based calculations, blood flow-related simulations with or without surrounding organs of the PTV, or deep learning-based models. One notable blood flow model is Beekman et al.'s stochastic model that simulates systemic blood flow in the human body based on a previously designed compartmental model applicable to any anatomical site.[41] This model is more explicitly grounded in flow physics than our approach, and also requires registration of each patient's anatomy with a phantom vasculature to predict blood dose. The latter step requires great precision when registering the thorax anatomy (which encompasses a large volume of low-dose regions) with smaller critical organs such as the aorta, especially as blood flow rates vary so much between great vessels and the rest of the body. This increased complexity allowed them to study effects such as patient breathing which our model neglects, but it comes at the cost of significantly longer runtimes (Beekman: 64 s to model blood flow and 61 s to accumulate dose on an M1 iMac with a time step of 0.05 s. Ours: 38 s end-to-end on an Intel Xeon E5-2630 Processor with a time step of ∼ 0.03 s for the blood-rich organs). Our stochastic approach to model flow through lower-dose organs in the thorax is aimed to be accurate on average over the course of a treatment. Indeed, Beekman et al. found that changes to blood dose due to breathing tended to average out and be negligible. Our model also avoids concerns with registering a phantom volume by using each patient's specific anatomy. Finally, our model uses the blood dose distribution to predict a post-treatment ALC, which accounts for time-dependent lymphocyte death and regeneration. By linking blood dose to cell kill and validating our predictions for the first time, using SBRT patient data for absolute lymphocyte reduction, we demonstrate the applicability of the model for mitigating RIIS.

Simpler models that use mean organ doses and subsets of organs in the thorax to compute immune suppression may have even shorter evaluation times, but will have less predictive power according to Beekman et al.[41] Other recent models have examined ALC reduction in RT treatments with standard fractionation. Jin et al. specifically examined RT for pancreatic and used DVH information to make their predictions,[34] rather than the three-dimensional dose maps that informed our dynamic dose delivery simulation. Ebrahami et al. developed a hybrid deep learning model for esophageal cancer.[37] Both models have limited use for SBRT, where the time-dependent immune suppression is not smoothly varying as in standard fractionation.

In addition to predicting lymphocyte depletion from Lung SBRT, this model also provides tools to potentially mitigate its immunosuppressive impact without altering efficacy. With near-real time predictive abilities, this model could interface with treatment planning systems, to predict lymphocyte depletions for prospective plans, these could be evaluated alongside traditional organ-at-risk dose metrics in determining a plan's quality. Furthermore, the analysis of dose-dependent lymphocyte kill contributions can link specific treatment plan

characteristics with lymphocyte depletion and help identify general techniques that may reduce it. After creating an initial treatment plan, one can estimate the total lymphocyte toxicity stemming from specific blood-dose levels (i.e., whether the majority of lymphotoxicity from the plan is due to a large volume of blood receiving a small dose or a smaller volume receiving a higher dose). This information can then be used to prioritize physical dose levels (i.e., standard RT planned doses) to minimize overall cell kill. This method is being evaluated prospectively in an NCI-funded clinical trial (NCT04273893).[56] One potential application of this model will be to optimize fractionation strategies from an immune perspective. Accounting for time-dependent lymphocyte reduction following RT may also help elucidate optimal timing for combined radiation and immunotherapy.

The results presented in this study already point to a few potentially important ways to reduce lymphotoxicity. For example, we found that patients with centrally located tumors experience a similar degree of lymphocyte depletion as patients with peripheral tumors despite being treated with 20% lower prescription doses (50 vs. 60 Gy). This counterintuitive finding, though agrees with the patient measurements, likely stems from differences in specifics of the dose distributions in these cases. Treatment plans for centrally located tumors deliver larger doses to blood-rich organs in the thorax (i.e., the great vessels and heart) resulting in more CLs accumulating a toxic dose per unit dose to the tumor. Developing treatment plans for centrally located tumors that explicitly avoid blood-rich areas may bring these situations closer to parity.

This study did have some limitations. The translation from blood dose to cell kill was estimated using in vitro data as in vivo lympho-toxicity data are not readily available. Lymphocyte subtypes (B cell, T cell, CD4+, CD8+, Tregs, and natural killer cells) have different impacts on tumor infiltration[57] and cancer prognosis. Additionally, their radiation sensitivity,[58] cell cycle stage,[59] and RIIS[60] could be different. We have currently assumed equal radio-sensitivities of lymphocyte sub types within the model. However, during the NCT04273893 trial, we acquired these sub type data with the intent of adding sub type predictions to the existing model in the future using the present study as a benchmark. The current version of the model did not discriminate the stationary lymphocyte populations in bony anatomy such as the thoracic spine or in lymphatic organs such as lymph nodes/vessels, special lymphatic organs such as thymus (relevant for patients younger than 20 years), GI/GU tract (not relevant for lung irradiation). Each of these subpopulations were treated as "other organs." Other patient-dependent factors such as age, race, smoking status that could have an impact on lymphocyte recovery were also not taken into account. Including these factors such as patient-specific time-dependent

immune suppression and recovery via osmosis between primary, secondary lymphoid organs and the blood circulation, lymphocyte rate of recovery will be a focus of a future study. Furthermore, all analysis was performed on planned dose distributions and thus uncertainties in patient alignment were not considered. However, the model's predictive power and speed makes it a promising candidate for decision making at the planning stage in the immune toxicity. This model is currently being used for treatment plan decision making at our institution in a clinical trial setting in order to reduce RIIS while maintaining highly conformal RTOG 0813/0915 criteria.

5 | CONCLUSION

We present a model that accurately predicts lymphocyte depletion following Lung SBRT as well as the onset of lymphopenia in a cohort of 64 patients under ten-fold cross validation. This model with ~38-s end-to-end prediction time has the capability to be interfaced with treatment planning systems to prospectively reduce immune cell toxicity without compromising treatment efficacy during treatment planning. Our proposed RIIS prediction method is adaptable to predict RIIS in other dose fractionations in the lung as well as other disease sites.

CONFLICT OF INTEREST STATEMENT
The authors declare no conflicts of interest.

REFERENCES

1. Crabtree TD, Denlinger CE, Meyers BF, et al. Stereotactic body radiation therapy versus surgical resection for stage I non–small cell lung cancer. *J Thora Cardiovasc Surg*. 2010;140(2):377-386. doi:10.1016/j.jtcvs.2009.12.054

2. Lee Y, Auh SL, Wang Y, et al. Therapeutic effects of ablative radiation on local tumor require CD8+ T cells: changing strategies for cancer treatment. *Blood*. 2009;114(3):589-595. doi:10.1182/blood-2009-02-206870

3. Schaue D, Ratikan JA, Iwamoto KS, McBride WH. Maximizing tumor immunity with fractionated radiation. *Int J Radiat Oncol Biol Phys*. 2012;83(4):1306-1310. doi:10.1016/j.ijrobp.2011.09.049

4. Ohba K, Omagari K, Nakamura T, et al. Abscopal regression of hepatocellular carcinoma after radiotherapy for bone metastasis. *BMJ*. 1998;43(4):575-577. doi:10.1136/gut.43.4.575

5. Deschoolmeester V, Baay M, Van Marck E, et al. Tumor infiltrating lymphocytes: an intriguing player in the survival of colorectal cancer patients. *BMC Immunol*. 2010;11(1):1-2. doi:10.1186/1471-2172-11-19

6. Pagès F, Galon J, Dieu-Nosjean M-C, Tartour E, Sautès-Fridman C, Fridman W-H. Immune infiltration in human tumors: a prognostic factor that should not be ignored. *Oncogene*. 2009;29(8):1093-1102. doi:10.1038/onc.2009.416

7. Kawai O, Ishii G, Kubota K, et al. Predominant infiltration of macrophages and CD8+T cells in cancer nests is a significant predictor of survival in stage IV nonsmall cell lung cancer. *Cancer*. 2008;113(6):1387-1395. doi:10.1002/cncr.23712

8. Dieu-Nosjean MC, Antoine M, Danel C, et al. Long-term survival for patients with non–small-cell lung cancer with intratumoral lymphoid structures. *J Clin Oncol*. 2008;26(27):4410-4417. doi:10.1200/jco.2007.15.0284

9. Grutters JPC, Kessels AGH, Pijls-Johannesma M, De Ruysscher D, Joore MA, Lambin P. Comparison of the effectiveness of radiotherapy with photons, protons and carbon-ions for non-small cell lung cancer: a meta-analysis. *Radiother Oncol*. 2010;95(1):32-40. doi:10.1016/j.radonc.2009.08.003

10. Tang C, Liao Z, Gomez D, et al. Lymphopenia association with gross tumor volume and lung V5 and its effects on non-small cell lung cancer patient outcomes. *Int J RadiatOncol Biol Phys*. 2014;89(5):1084-1091. doi:10.1016/j.ijrobp.2014.04.025

11. Contreras J, Lin A, Weiner AA, et al. Cardiac dose is associated with immunosuppression and poor survival in locally advanced non-small cell lung cancer. *Radiother Oncol*. 2018;128(3):498-504. doi:10.1016/j.radonc.2018.05.017

12. Balmanoukian A, Ye X, Herman J, Laheru D, Grossman SA. The association between treatment-related lymphopenia and survival in newly diagnosed patients with resected adenocarcinoma of the pancreas. *Cancer Invest*. 2012;30(8):571-576. doi:10.3109/07357907.2012.700987

13. Venkatesulu BP, Mallick S, Lin SH, Krishnan S. A systematic review of the influence of radiation-induced lymphopenia on survival outcomes in solid tumors. *Crit Rev Oncol Hematol*. 2018;123:42-51. doi:10.1016/j.critrevonc.2018.01.003

14. Grossman SA, Ye X, Lesser G, et al. Immunosuppression in patients with high-grade gliomas treated with radiation and temozolomide. *Clin Cancer Res*. 2011;17(16):5473-5480. doi:10.1158/1078-0432.ccr-11-0774

15. Leoncini E, Ricciardi W, Cadoni G, et al. Adult height and head and neck cancer: a pooled analysis within the INHANCE Consortium. *Eur J Epidemiol*. 2013;29(1):35-48. doi:10.1007/s10654-013-9863-2

16. Campian JL, Ye X, Brock M, Grossman SA. Treatment-related lymphopenia in patients with Stage III non-small-cell lung cancer. *Cancer Invest*. 2013;31(3):183-188. doi:10.3109/07357907.2013.767342

17. Wild AT, Ye X, Ellsworth SG, et al. The association between chemoradiation-related lymphopenia and clinical outcomes in patients with locally advanced pancreatic adenocarcinoma. *Am J Clin Oncol*. 2015;38(3):259-265. doi:10.1097/coc.0b013e3182940ff9

18. Grossman SA, Ellsworth S, Campian J, et al. Survival in patients with severe lymphopenia following treatment with radiation and chemotherapy for newly diagnosed solid tumors. *J Natl Compr Cancer Netw*. 2015;13(10):1225-1231. doi:10.6004/jnccn.2015.0151

19. Campian JL, Sarai G, Ye X, Marur S, Grossman SA. Association between severe treatment-related lymphopenia and progression-free survival in patients with newly diagnosed squamous cell head and neck cancer. *Head Neck*. 2014;36(12):1747-1753. doi:10.1002/hed.23535

20. Chang JY, Lin SH, Dong W, et al. Stereotactic ablative radiotherapy with or without immunotherapy for early-stage or isolated lung parenchymal recurrent node-negative non-small-cell lung cancer: an open-label, randomised, phase 2 trial. *Lancet*. 2023;402(10405):871-881. doi:10.1016/s0140-6736(23)01384-3

21. Ménétrier-Caux C, Ray-Coquard I, Blay JY, Caux C. Lymphopenia in cancer patients and its effects on response to immunotherapy: an opportunity for combination with cytokines? *J Immunother Cancer*. 2019;7(1):1-15. doi:10.1186/s40425-019-0549-5

22. Zhao X, Li J, Zheng L, et al. Immune response on optimal timing and fractionation dose for hypofractionated radiotherapy in non–small-cell lung cancer. *Front Mol Biosci*. 2022;9:786864. doi:10.3389/fmolb.2022.786864

23. Zhang J, Yang L, Li H, et al. Dosimetric effect of thymus and thoracic duct on radiation-induced lymphopenia in patients with primary lung cancer who received thoracic radiation. *Adv Radiat Oncol*. 2023:101260. doi:10.1016/j.adro.2023.101260

24. Abravan A, Faivre-Finn C, Kennedy J, McWilliam A, van HM. Radiotherapy-related lymphopenia affects overall survival in patients with lung cancer. *J Thorac Oncol*. 2020;15(10):1624-1635. doi:10.1016/j.jtho.2020.06.008

25. Lambin P, Lieverse RIY, Eckert F, et al. Lymphocyte-sparing radiotherapy: the rationale for protecting lymphocyte-rich organs when combining radiotherapy with immunotherapy. *Semin Radiat Oncol*. 2020;30(2):187-193. doi:10.1016/j.semradonc.2019.12.003

26. Maehata Y, Onishi H, Kuriyama K, et al. Immune responses following stereotactic body radiotherapy for Stage I primary lung cancer. *BioMed Res Int*. 2013;2013:1-11. doi:10.1155/2013/731346

27. Zhao Q, Li T, Chen G, Zeng Z, He J. Prognosis and risk factors of radiation-induced lymphopenia in early-stage lung cancer treated with stereotactic body radiation therapy. *Front Oncol*. 2020;9:1488. doi:10.3389/fonc.2019.01488

28. McMullen T, Liyanage S, Alonso C, Wijesooriya K. *Radiation related lymphopenia for lung SBRT treatments: measurement versus simulation*. Wiley; 2017:3118-3118.

29. Weeke E. The development of lymphopenia in uremic patients undergoing extracorporeal irradiation of the blood with portable beta units. *Radiat Res*. 1973;56(3):554-559. doi:10.2307/3573724

30. Maclennan IC, Kay HE. Analysis of treatment in childhood leukemia. IV. The critical association between dose fractionation and immunosuppression induced by cranial irradiation. *Cancer*. 1978;41(1):108-111. doi:10.1002/1097-0142(197801)41:1⟨108::AID-CNCR2820410116⟩3.0.CO;2-Z

31. Wild AT, Herman JM, Dholakia AS, et al. Lymphocyte-sparing effect of stereotactic body radiation therapy in patients with unresectable pancreatic cancer. *Int J Radiat Oncol Biol Phys*. 2016;94(3):571-579. doi:10.1016/j.ijrobp.2015.11.026

32. Yovino S, Kleinberg L, Grossman SA, Narayanan M, For E. The etiology of treatment-related lymphopenia in patients with malignant gliomas: modeling radiation dose to circulating lymphocytes explains clinical observations and suggests methods of modifying the impact of radiation on immune cells. *Cancer Invest*. 2013;31(2):140-144. doi:10.3109/07357907.2012.762780

33. Shin J, Xing S, McCullum L, et al. HEDOS—a computational tool to assess radiation dose to circulating blood cells during external beam radiotherapy based on whole-body blood flow simulations. *Phys Med Biol*. 2021;66(16):164001. doi:10.1088/1361-6560/ac16ea

34. Jin JY, Mereniuk T, Yalamanchali A, et al. A framework for modeling radiation induced lymphopenia in radiotherapy. *Radiother Oncol*. 2020;144:105-113. doi:10.1016/j.radonc.2019.11.014

35. Basler L, Andratschke N, Ehrbar S, Guckenberger M, Tanadini-Lang S. Modelling the immunosuppressive effect of liver SBRT by simulating the dose to circulating lymphocytes: an in-silico planning study. *Radiat Oncol*. 2018;13(1):1-8. doi:10.1186/s13014-018-0952-y

36. Xing S, Shin J, Pursley J, et al. A dynamic blood flow model to compute absorbed dose to circulating blood and lymphocytes in liver external beam radiotherapy. *Phys Med Biol*. 2022;67(4):045010. doi:10.1088/1361-6560/ac4da4

37. Ebrahimi S, Lim GJ, Hobbs BP, Lin SH, Mohan R, Cao W. A hybrid deep learning model for forecasting lymphocyte depletion during radiation therapy. *Med Phys*. 2022;49(5):3507-3522. doi:10.1002/mp.15584

38. Hammi A, Paganetti H, Grassberger C. 4D blood flow model for dose calculation to circulating blood and lymphocytes. *Phys Med Biol*. 2020;65(5):055008. doi:10.1088/1361-6560/ab6c41

39. Grassberger C, Paganetti H. Methodologies in the modeling of combined chemo-radiation treatments. *Phys Med Biol*. 2016;61(21):R344-R367. doi:10.1088/0031-9155/61/21/r344

40. Grassberger C, Scott JG, Paganetti H. Biomathematical optimization of radiation therapy in the era of targeted agents. *Int J Radiat Oncol Biol Phys*. 2017;97(1):13-17. doi:10.1016/j.ijrobp.2016.09.008

41. Beekman C, Withrow JD, Alfonso CM, et al. A stochastic model of blood flow to calculate blood dose during radiotherapy. *Phys Med Biol*. 2023;68(22):225007. doi:10.1088/1361-6560/ad02d6

42. Jin JY, Hu C, Xiao Y, et al. Higher radiation dose to the immune cells correlates with worse tumor control and overall survival in patients with Stage III NSCLC: a secondary analysis of RTOG0617. *Cancers*. 2021;13(24):6193. doi:10.3390/cancers13246193

43. Ladbury CJ, Rusthoven CG, Camidge DR, Kavanagh BD, Nath SK. Impact of radiation dose to the host immune system on tumor control and survival for Stage III non-small cell lung cancer treated with definitive radiation therapy. *Int J Radiat Oncol Biol Phys*. 2019;105(2):346-355. doi:10.1016/j.ijrobp.2019.05.064

44. Thor M, Deasy JO, Hu C, et al. Modeling the impact of cardiopulmonary irradiation on overall survival in NRG Oncology Trial RTOG 0617. *Clin Cancer Res*. 2020;26(17):4643-4650. doi:10.1158/1078-0432.ccr-19-2627

45. Leggett RW, Williams LR. A proposed blood circulation model for reference man. *Health Phys*. 1995;69(2):187-201. doi:10.1097/00004032-199508000-00003

46. Williams LR, Leggett RW. Reference values for resting blood flow to organs of man. *Clin Phys Physiol Measure*. 1989;10(3):187-217. doi:10.1088/0143-0815/10/3/001

47. Nakamura N, Kusunoki Y, Akiyama M. Radiosensitivity of CD4 or CD8 positive human T-lymphocytes by an in vitro colony formation assay. *Radiat Res*. 1990;123(2):224-227. doi:10.2307/3577549

48. Gabe IT, Gault JH, Ross J, et al. Measurement of instantaneous blood flow velocity and Pressure in Conscious Man with a catheter-tip velocity probe. *Circulation*. 1969;40(5):603-614. doi:10.1161/01.cir.40.5.603

49. Sharp PF. The measurement of blood flow in humans using radioactive tracers. *Physiol Measure*. 1994;15(4):339-379. doi:10.1088/0967-3334/15/4/001

50. McMahon SJ. The linear quadratic model: usage, interpretation and challenges. *Phys Med Biol*. 2018;64(1):01TR01. doi:10.1088/1361-6560/aaf26a

51. Wijesooriya K, Colen J, McMullen T, Liyanage S, et al. Clinical significance of treatment related lymphopenia in lung SBRT and a method to ameliorate them. *Radiother Oncol*. 2019;133(Supplement 1):S406-S407. doi:10.1016/S0167-8140(19)31205-8

52. Swanson GP, Hammonds K, Jhavar S. Lymphocyte response and recovery to radiation therapy alone. *Ann Blood*. 2023;8. doi:https://doi.org/10.21037/aob-21-74

53. Videtic GM, Hu C, Singh A, et al. Radiation Therapy Oncology Group (RTOG) Protocol 0915: a randomized phase 2 study comparing 2 stereotactic body radiation therapy (SBRT) schedules for medically inoperable patients with Stage I peripheral non-small cell lung cancer. *Int J Radiat Oncol Biol Phys*. 2013;87(2):S3. doi:10.1016/j.ijrobp.2013.06.016

54. Bezjak A, Papiez L, Bradley J, et al. Radiation Therapy Oncology Group RTOG 0813 seamless Phase I/II study of stereotactic lung radiotherapy (SBRT) For early stage, centrally located, nonsmall cell lung cancer (NSCLC) in medically inoperable patients. *Update*. 2009. https://pps4rt.com/wp-content/uploads/2019/07/RTOG-0813.pdf

55. Ellsworth SG. Field size effects on the risk and severity of treatment-induced lymphopenia in patients undergoing radiation therapy for solid tumors. *Adv Radiat Oncol*. 2018;3(4):512-519. doi:10.1016/j.adro.2018.08.014

56. https://clinicaltrials.gov/study/NCT04273893

57. Chen Y, Jin Y, Hu X, Chen M. Infiltrating T lymphocytes in the tumor microenvironment of small cell lung cancer: a state of knowledge review. *J Cancer Res ClinOncol*. 2022;148(4):881-895. doi:10.1007/s00432-021-03895-x

58. Swerdlow SH, Campo E, Pileri SA, et al. The 2016 revision of the World Health Organization classification of lymphoid neoplasms. *Blood*. 2016;127(20):2375-2390. doi:10.1182/blood-2016-01-643569

59. Paganetti H. A review on lymphocyte radiosensitivity and its impact on radiotherapy. *Front Oncol*. 2023;13. doi:10.3389/fonc.2023.1201500

60. Thierens HMA, Vral AM, Van Haelst JP, et al. Lymphocyte labeling with technetium-99m-HMPAO: a radiotoxicity study using the micronucleus assay. *J Nucl Med*. 1992;33(6):1167-1174. https://jnm.snmjournals.org/content/jnumed/33/6/1167.full.pdf